Influences of Experimental Parameters on Chemical Exchange Saturation Transfer (CEST) Metrics of Brain Tumors Using Animal Models at 4.7 T

Hye-Young Heo[1,2], **Yi Zhang**[1,3], **Shanshan Jiang**[1], and **Jinyuan Zhou**[1,2]

[1]Divison of MR Research, Department of Radiology, Johns Hopkins University, Baltimore, Maryland, USA

[2]F.M. Kirby Research Center for Functional Brain Imaging, Kennedy Krieger Institute, Baltimore, Maryland, USA

[3]Key Laboratory for Biomedical Engineering of Ministry of Education, College of Biomedical Engineering & Instrument Science, Zhejiang University, Hangzhou, China

Abstract

Purpose—To investigate the dependence of magnetization-transfer-ratio-asymmetry at 3.5 ppm (MTR_{asym}(3.5ppm)), quantitative amide-proton-transfer ($APT^{\#}$), and nuclear-Overhauser-enhancement ($NOE^{\#}$) signals or contrasts on experimental imaging parameters.

Methods—Modified Bloch equation-based simulations using two-pool and five-pool exchange models, and *in-vivo* rat brain tumor experiments at 4.7 T were performed, with varied radiofrequency (RF) saturation power levels, saturation lengths, and relaxation delays. The MTR_{asym}(3.5ppm), $APT^{\#}$, and $NOE^{\#}$ contrasts between tumor and normal tissues were compared among different experimental parameters.

Results—The MTR_{asym}(3.5ppm) image contrasts between tumor and normal tissues initially increased with the RF saturation length, and the maxima occurred at 1.6–2 s under relatively high RF saturation powers (> 2.1 μT) and at a longer saturation length under relatively low RF saturation powers (< 1.3 μT). The $APT^{\#}$ contrasts also increased with the RF saturation length but peaked at longer RF saturation lengths relative to MTR_{asym}(3.5ppm). The $NOE^{\#}$ contrasts were either positive or negative, depending on the experimental parameters applied.

Conclusion—Tumor MTR_{asym}(3.5ppm), $APT^{\#}$, and $NOE^{\#}$ contrasts can be maximized at different saturation parameters. The maximum MTR_{asym}(3.5ppm) contrast can be obtained with a relatively longer RF saturation length (several seconds) at a relatively lower RF saturation power.

Keywords

CEST; APT; RF saturation length; RF saturation power; brain tumor

Corresponding and Reprint Author: Hye-Young Heo, Ph.D., Division of MR Research, Department of Radiology, Johns Hopkins University School of Medicine, 600 N. Wolfe Street, Park 334, Baltimore, MD 21287, USA. Phone: (+1-410) 955-9498, Fax: (+1-410) 614-1977, hheo1@jhmi.edu.

INTRODUCTION

Chemical exchange saturation transfer (CEST) imaging is a promising molecular MRI technique that provides unique contrast based on the proton exchange between bulk water protons and solute labile protons (1). Using CEST MRI, endogenous or exogenous low-concentration mobile biomolecules with water-exchangeable labile protons can be selectively detected indirectly through the bulk water signal used for clinical imaging (2–4). Notably, amide proton transfer (APT) imaging, a variant of CEST MRI, is based on the chemical exchange between free bulk water protons and the amide protons (-NH) of endogenous mobile proteins and peptides (5, 6). Early clinical data suggest that APT-weighted (APTw) imaging has unique features by which to detect and characterize strokes (7–10), brain tumors (11–16), prostate cancer (17), head and neck cancer (18), and many other human diseases (19–21). Notably, it has been shown clearly that APTw MRI has excellent potential to differentiate brain tumors from peritumoral edema or normal tissue, high-grade from low-grade tumors, or treatment-related damage from tumor recurrence (22–24), as well as to predict genomic markers in gliomas, such as the isocitrate dehydrogenase mutation status and O6-methylguanine-DNA methyltransferase promoter methylation status (25, 26).

Theoretically, the APT effect is usually measured by subtraction of the magnetization transfer ratio (MTR) of the reference image at −3.5 ppm upfield, with respect to water, from that of the label image at +3.5 ppm downfield to remove direct radiofrequency (RF) water saturation (DS, also called spillover), and broad semisolid macromolecular magnetization transfer contrast (MTC) effects (5). The standard asymmetry analysis of Z-spectrum mixes the information from the intramolecular and intermolecular upfield nuclear Overhauser enhancement (NOE) signals of mobile proteins, lipids, and metabolites in tissue (27–33). Moreover, the effects of the different proton pools are non-linearly added in the Z-spectrum, particularly at high RF saturation power levels. Therefore, the MTR_{asym}(3.5ppm) images obtained are usually called APTw images (11). Nevertheless, it has been shown recently that high APTw signal intensity in malignant gliomas is dominated by the APT effect (34–37). Consequently, APT image signals and contrast measured by MTR asymmetry analysis should be carefully interpreted in clinical applications.

Based on a simplified two-pool exchange model (not MTC, the RF saturation applied to only the amide proton pool with the water proton pool unperturbed), the amide proton transfer ratio (APTR) can be approximately given by (2, 3, 38):

$$APTR = \frac{k_{s_1 w}[amide\ protons]}{R_{1w}[water\ protons]} \cdot \alpha \cdot (1 - e^{-TsR_{1w}}), \alpha = \frac{(\gamma B_1)^2}{(\gamma B_1)^2 + k_{s_1 w}^2} \quad [1]$$

where k_{s1w} is the proton exchange rate from the amide proton pool (s_1) to the free water proton pool (w), R_{1w} (= $1/T_{1w}$) is the longitudinal relaxation rate of water, square brackets ([…]) denote the concentration, α is the RF saturation efficiency, B_1 is the RF saturation

power, and Ts is the length of the saturation time. Based on Eq. [1], APTR increases with the RF saturation length because it allows more accumulation of saturated protons in free water protons, and reaches a steady state. At $B_1 = 1 - 2 \mu T$ ($\alpha \approx 0.99$), an APTR with a Ts of 1 s and 2 s has a 51% and 76% of steady-state APTR contrast using a T_{1w} of 1.4 s, a k_{s1w} of 29 Hz, [amide protons] of 72 mM, and [water protons] of 111 M. However, it is important to realize that this simple analytical approximation may not be suitable in the presence of the conventional MTC effect in tissue (37, 39). In the *in-vivo* study, the application of an elongated RF saturation under strong RF saturation may reduce (rather than increase) APTw signals due to higher dilution effects from semisolid MTC and spillover when MTR asymmetry analysis is used.

Conventional APT imaging studies have used a moderate repetition time (TR) or relaxation delay (magnetization recovery time) to reduce the scan time. A steady-state water longitudinal magnetization (M_z^w) is reduced when a short relaxation delay, compared to T_1 relaxation time, is applied, resulting in a decrease in initial water signal reduction and the APT effect (40). Therefore, APT experimental imaging parameters must be optimized based on a combination of the RF saturation power level, the RF saturation length, and the relaxation delay to maximize APTw signal intensities or/and tumor contrasts. Here, we investigated the dependence of APTw, quantitative APT (APT#), and NOE (NOE#) signals using extrapolated semisolid MT reference (EMR) signals (35, 36) on the CEST experimental imaging parameters at 4.7 T using modified Bloch equation-based simulations and rat brain tumor models.

METHODS

Bloch-McConnell Simulations

Modified Bloch-McConnell equation-based simulations were performed to simulate CEST effects, as described in (35, 36, 41, 42). The five-pool exchange model, including the free bulk water (*w*), amide (s_1), NOE-related (s_2), CEST@2ppm (s_3), and semisolid MTC (*m*) proton pools, was used. Note that many previous studies have observed CEST peaks around 2 ppm caused by multiple underlying components such as side-chain amide or guanidinium protons of proteins and peptides, and guanidinium protons in creatine. The exchange model and the magnetization in each pool (M^w, M^{s1}, M^{s2}, M^{s3}, and M^m) in the presence of proton exchange and RF saturation, can be written in a matrix format:

$$\frac{dM(t)}{dt} = A \cdot M(t) + b \quad [2]$$

where

$$A = \begin{bmatrix} D_w & N_{ws_1} & N_{ws_2} & N_{ws_3} & N_{wm} \\ N_{s_1w} & D_{s_1} & N_{s_1s_2} & N_{s_1s_3} & N_{s_1m} \\ N_{s_2w} & N_{s_2s_1} & D_{s_2} & N_{s_2s_3} & N_{s_2m} \\ N_{s_3w} & N_{s_3s_1} & N_{s_3s_2} & D_{s_3} & N_{s_3m} \\ N_{mw} & N_{ms_1} & N_{ms_2} & N_{ms_3} & D_m \end{bmatrix} \quad [3]$$

$$D_i = \begin{bmatrix} -k_{2i} & -(\omega - \omega_i) & 0 \\ (\omega - \omega_i) & -k_{2i} & -\omega_1 \\ 0 & \omega_1 & -k_{1i} \end{bmatrix} \quad [4]$$

$$N_{ij} = k_{ij} \begin{bmatrix} 1 & 0 & 0 \\ 0 & 1 & 0 \\ 0 & 0 & 1 \end{bmatrix} \quad [5]$$

$$b = \begin{bmatrix} b_w & b_{s_1} & b_{s_2} & b_{s_3} & b_m \end{bmatrix}^T \quad [6]$$

$$b_i = \begin{bmatrix} 0 & 0 & M_0^i R_{1i} \end{bmatrix}^T \quad [7]$$

where $i = w, S_1, S_2, S_3,$ and m; ω_i is the resonance frequency of pool i; ω_1 is the RF saturation amplitude; ω is the RF saturation frequency; k_{ij} is the proton exchange rate from pool i to pool j; R_{1i} and R_{2i} are the longitudinal and transverse relaxation rate of pool i, respectively; $k_{1/2w}, k_{1/2s1}, k_{1/2s2}, k_{1/2s3}, k_{1/2m}$ are given by $R_{1/2w}+k_{ws1}+k_{ws2}+k_{ws3}+k_{wm}$, $R_{1/2s1}+k_{s1w}, R_{1/2s2}+k_{s2w}, R_{1/2s3}+k_{s3w},$ and $R_{1/2m}+k_{mw}$, respectively; and M_0^i is the equilibrium magnetization of pool i. The linear coupled equations (Eq. [2]) can be analytically solved by:

$$M = (M_0 + bA^{-1})e^{At} - bA^{-1} \quad [8]$$

where

$$M_0 = \left[M_0^{w'} \; M_0^{s_1'} \; M_0^{s_2'} \; M_0^{s_3'} \; M_0^{m'} \right]^T \quad [9]$$

$$M_0^{i'} = \left[0 \; 0 \; M_0^{i} \right]^T \quad [10]$$

Longitudinal magnetization evolutions were simulated based on a continuous-wave (CW) CEST sequence with a single-shot spin-echo EPI readout or a pulse-train CEST sequence with a single-shot turbo spin-echo (TSE) readout. One TR consists of off-resonance RF saturation followed by image acquisition, and relaxation delay (Fig. 1a). For the saturation preparation, varied RF saturation powers, B_1 (ω_1 in units of rad/s, Eq. [4]) and saturation lengths, Ts (t in units of s, Eq. [8]) were applied. In the case of the pulse-train saturation (a series of four block pulses, 200 ms duration each), crusher gradients of 10 ms duration were applied between block RF saturation pulses to suppress residual transverse magnetization by setting zero transverse magnetization components (spoiler matrix). For the image acquisition, the magnetization vector evolution was computed by multiplying the previous magnetization vectors with the rotation matrices to account for a 90° excitation pulse followed by a 180° refocusing pulse or multiple refocusing pulses forming echo trains. During the relaxation delay period, the magnetization vector was computed solely by relaxation recovery process in the absence of B_1. The five-pool exchange model can be reduced to the two-pool APT exchange model (free bulk water + amide proton pools) or the two-pool MTC exchange model (free bulk water + semisolid MTC proton pools) by assuming the concentration of other proton pools to be zero. In addition, the fifteen ordinary differential Bloch equations were numerically solved with the relative tolerance values of 10^{-7} to display the evolution of the longitudinal magnetization vector of the free bulk water during the entire Z-spectrum acquisition.

After five dummy scans, Z-spectra were generated at RF saturation frequency offsets ranging from −6 to +6 ppm with RF saturation power levels (B_1) of 0.5, 1.3, 2.1, and 2.9 μT; RF saturation lengths (Ts) of 0.2, 0.4, 0.6, 0.8, 1, 1.2, 1.4, 1.6, 1.8, 2, 3, 4, and 6 s; relaxation delays (Td) of 0.5, 1, 1.5, 1.94 (≈ 2), 3.94 (≈ 4), 5.94 (≈ 6), and 8 s; and an image acquisition time (Ta) of 60 ms. TR was equal to the sum of the RF saturation length, image acquisition time, and relaxation delay (TR = Ts + Ta + Td). Model parameters used for simulations were as follows (normal/tumor): fractional pool sizes of amide, NOE, CEST@2ppm, and semisolid MTC relative to water protons were 0.21%/0.39%, 1.48%/0.93%, 0.06%/0.059%, and 7.5%/3.1%; T_1 values of water, amide, NOE, CEST@2ppm, and semisolid MTC were 1.53/1.95 s, 1.4/1.8 s, 1.4/1.8 s, 1.4/1.8 s, and 1.4/1.8 s; T_2 values of water, amide, NOE, CEST@2ppm, and semisolid MTC were 56.0/72.0 ms (43), 3.98/2.50 ms, 0.37/0.48 ms, 3.91/2.12 ms, and 19/19 μs; exchange rates of amide, NOE, CEST@2ppm, and semisolid MTC relative to water protons were 29 Hz, 11 Hz, 440 Hz, and 22 Hz; and chemical shifts of amide, NOE, CEST@2ppm, and semisolid MTC from water were 3.5 ppm, −3.5 ppm, 2 ppm, and 0 ppm, respectively. These parameters (except T_{2w}) were determined by a five-pool exchange, model-fitting procedure using rat tumor models

(Supporting Figs. S1–2). In addition, we investigated the influence of water T_1 effect on MTR_{asym}(3.5ppm), $APT^{\#}$, and $NOE^{\#}$ tumor contrasts with CW-CEST EPI sequence at 4.7 T and pulse-train CEST TSE sequence at 3 T. For Bloch simulation at 3 T (36, 37, 44), all T_1 values (normal/tumor) were set at 1.2/1.4 s; T_2 values of water (normal/tumor) were set at 80.0/100.0 ms. Other parameters were the same as for the parameters at 4.7 T. Another compartment was included in the simulation mimicking edema tissues. For convenience, water T_1 and T_2 values of edema were same as for tumor case; but other parameters were identical to those used in the normal case.

Monte Carlo Simulations

We performed comprehensive Monte Carlo simulations to evaluate the accuracy and precision of the estimated tumor contrast of the CEST metrics with different RF saturation parameters and relaxation delays, under realistic noise conditions. With each combination of the saturation parameters (B_1, Ts, and Td), the noise-free ground truth contrast map (= tumor − normal) and 1000 sets of noisy (based on a Rician distribution) contrast maps were simulated. For such a Rician distribution, we estimated an apparent standard deviation of ~42.9 (scaled by a factor of 1/0.655 to account for the Rician noise distribution (45)) from a background region and an average signal of ~12015 from a tumor region in saturated images at 3.5 ppm (SNR of ~280). For each trial, the pseudo-random Rician noise samples were generated by using conventional inverse transform sampling, and pool parameters in the five-pool model and the apparent standard deviation were randomly chosen within ± 1% range. The standard deviation from 1000 trials and mean deviation from the ground truth were calculated for the precision and accuracy of the estimated tumor contrast.

In-vivo MRI Experiments

All MR experiments were performed on a 4.7 T animal MRI system (Bruker Biospin, Billerica, Massachusetts) with an actively decoupled cross-coil set-up, which consisted of a 7-cm body coil for RF transmission and a 2.5-cm surface coil for signal reception. Six tumor-bearing Fischer 344 rats (male; adult) were scanned at ~12 days post-implantation. 25,000 9L gliosarcoma cells (obtained from the Brain Tumor Research Center, UCSF, CA, USA) in 2 ml media for each rat were stereotactically injected over 3–4 min. Animal care throughout the experimental procedures in the study was in accordance with institutional guidelines. Conventional high-resolution coronal T_2-weighted images were acquired with a fast spin-echo sequence to identify the tumor size and location and to set the position of following single-slice imaging, with the following parameters: TR = 3 s; echo time (TE) = 64 ms; field of view (FOV) = 32 × 32 mm^2; five slices; slice thickness = 1.5 mm; matrix = 192 × 192; averages = 2. A single slice passing through a largest tumor region with T_2-weighted hyperintensity was chosen for water T_1 (T_{1w}^{obs}), T_2 (T_{2w}^{obs}), apparent diffusion coefficient (ADC), and CEST imaging, as described previously (35, 37, 43).

CEST images were acquired using a fat-suppressed, spin-echo EPI pulse sequence, with a continuous wave (CW) RF saturation pulse and a single-shot EPI readout, with the following parameters: TE = 30 ms; matrix size = 64 × 64; FOV = 32 × 32 mm^2; spatial resolution = 0.5 × 0.5 mm^2; slice thickness = 1.5 mm; and single slice acquisition. TRs were varied according to RF saturation lengths and relaxation delays. For each RF saturation power level

of 1.3 µT or 2.1 µT, and each relaxation delay of 3.94 s (≈ 4 s) or 5.94 s (≈ 6 s), RF saturation lengths were varied at 0.4, 0.8, 1.2, 1.6, 2, 3, and 4 s (only for the relaxation delay of 6 s). The frequency sweep corresponded to the wide-range Z-spectrum with 62 frequency offsets: unsaturated (S_0), 0, ± 0.5, …, and ± 15 ppm, in intervals of 0.5 ppm for EMR fitting and quantification analysis. For B_0 corrections, water saturation shift-referencing (WASSR) images with 26 frequency offsets were acquired from +0.6 to −0.6 ppm at intervals of 0.05 ppm, including S_0, and an RF saturation power of 0.5 µT (46).

EMR Fitting and CEST Image Processing

All Bloch equation-based simulations and *in-vivo* CEST image analyses were performed using MATLAB (The MathWorks, Natick, Massachusetts). For *in-vivo* studies, CEST images were first normalized voxel-by-voxel by the corresponding S_0 image and then corrected for B_0 inhomogeneities using the WASSR method (46). Then, a two-pool MTC curve was generated using steady-state (35–37, 43) and non-steady-state EMR techniques. In the two-pool MTC model, it is assumed that the transverse magnetizations of the two pools (M_0^w and M_0^m) reach a steady-state at the end of the off-resonance RF irradiation (several hundreds of milliseconds) because both R_2^w and R_2^m are fast enough for their transverse magnetizations to reach zero. At steady-state condition, the time derivatives of the transverse magnetizations are equal to zero and the transverse magnetization terms can be rewritten as:

$$M_y^{w,m} = -\frac{R_{rfw,rfm}}{\omega_1} M_z^{w,m} \quad [11]$$

where the RF absorption rate, $RF_{rfw,rfm}$, is the loss rate of the longitudinal magnetization by the free bulk water and semisolid pool due to the off-resonance RF irradiation. The RF absorption rate is defined as:

$$R_{rfw,rfm} = \frac{\omega_1^2 (1/R_{2w,2m})}{1 + \left[(1/R_{2w,2m})(\omega_{w,m} - \omega)\right]^2} \quad [12]$$

where ω_w and ω_m are frequency offsets for free bulk water and semisolid pool, respectively. The differential equations for the longitudinal magnetization of the free bulk water pool from Eq. [2] – [7] can have the analytical solution as:

$$M_z^w(t) = A_1 e^{\lambda_1 t} + A_2 e^{\lambda_2 t} + M_{ss}^w \quad [13]$$

$$\lambda_{(1,2)} = -\frac{(R_1^w + R_1^m) + (k_{wm} + k_{mw}) + (R_{rfw} + R_{rfm})}{2}$$
$$\pm \frac{\sqrt{\left[(R_1^m - R_1^w) + (k_{mw} - k_{wm}) + (R_{rfm} - R_{rfw})\right]^2 + 4k_{mw}k_{wm}}}{2} \quad [14]$$

A_1 and A_2 are constants determined experimentally and $\lambda_{(1,2)}$ represents the longitudinal relaxation rates of the free bulk water pool under the saturation of the semisolid proton pool. If λ_2/λ_1 is high enough and A_2/A_1 approaches zero, Eq. [13] can be simplified to be (38, 47):

$$M_z^w(t) = (M_0^w - M_{ss}^w)e^{\lambda_1 t} + M_{ss}^w \quad [15]$$

where

$$M_{ss}^w = M_0^w \frac{R_{1m}(k_{mw}M_0^m/R_{1w}) + R_{rfm} + R_{1m} + k_{mw}}{(k_{mw}M_0^m/R_{1w})(R_{rfm} + R_{1m}) + \left[1 + (\omega_1/2\pi\Delta\omega)^2(R_{2w}/R_{1w})\right](R_{rfm} + R_{1m} + k_{mw})}$$

$$[16]$$

R_{rfm} is dependent on absorption super-Lorentzian lineshape, $g_m(2\pi\ \omega)$.

$$R_{rfm} = \omega_1^2 \pi g_m(2\pi\Delta\omega) \quad [17]$$

$$g_m(2\pi\Delta\omega) = \int_0^{\pi/2} d\theta \sin\theta \sqrt{\frac{2}{\pi}} \frac{1}{R_{2m}(3\cos^2\theta - 1)} e^{-2\left(\frac{2\pi\Delta\omega}{R_{2m}3\cos^2\theta - 1}\right)^2} \quad [18]$$

where θ is the dipole orientation angle between the magnetic moment and the external magnetic field.

Steady-state two-pool MTC model (Eq. [16]) for the CEST image obtained from long saturation times (Ts > 2 s) can be uniquely determined in terms of five combined parameters, k_{mw}, R_{1m}, R_{2m}, $k_{mw}M_0^m/R_{1w}$, and R_{2w}/R_{1w}. In addition, for non-steady-state MTC model (Eq. [15]), the observed water longitudinal relaxation rate (R_{1w}^{obs}) was determined from the inversion recovery MRI experiment and used to calculate the water longitudinal relaxation rate (R_{1w}) using the following equation (48, 49):

$$R_{1w} = R_{1w}^{obs} - \frac{k_{mw}M_0^m(R_{1m} - R_{1w}^{obs})}{R_{1m} - R_{1w}^{obs} + k_{mw}} \quad [19]$$

For the EMR calculation, the wide-frequency-offset semisolid MTC data between 15 and 7 ppm to avoid possible downfield CEST and upfield NOE contributions, and the data at the offset of 0.5 ppm to improve the fitting quality, were fitted to two-pool MTC exchange models with a super-Lorentzian line-shape, based on the nonlinear least-squares fitting method, which implemented the Levenberg-Marquardt algorithm. The Super-Lorentzian line-shape function was evaluated by the numerical integration. The Super-Lorentzian value was extrapolated from 200 Hz to an asymptotic limit at the zero offset when drawing MTC curves due to its on-resonance singularity. However, the singularity of the Super-Lorentzian line-shape was not issued during the MTC fitting because the wide-frequency offsets were not defined at on-resonance. The fitting quality using the estimated MTC model parameters was evaluated by the root of the sum of the squared differences between the fitted and experimental data, and a goodness-of-fit metric. In this fitting procedure, the M_w^0 was normalized to 1, and the longitudinal relaxation rate of semisolid MTC was fixed to be 0.7143 Hz (= 1/1.4 s) (50), because it is insensitive to the fitting procedure. Finally, by subtracting experimental data from the two-pool MTC models, APT$^{\#}$ and NOE$^{\#}$ signals were calculated and compared with the MTR$_{asym}$(3.5ppm) signals. Note that the large and broad symmetrical MTC is removed, and all other remain when the symmetric MTC model is used. Thus, a relatively clean APT$^{\#}$ signal can be measured, and the NOE$^{\#}$ signal includes both the local NOE (from mobile molecules) and the conventional MTR asymmetry (from relatively fewer mobile protons).

For other MRI parametric mappings, T_{1w}^{obs} was fitted using $I = A + Be^{-TI/T_{1w}^{obs}}$. T_{2w}^{obs} was fitted using $I = I_0 e^{-TE/T_{2w}^{obs}}$. The average ADC of water, $ADC_{av} = Trace(D)/3$, was fitted by $I = I_0 e^{-b \cdot ADC_{av}}$. To compare the MTR$_{asym}$(3.5ppm), APT$^{\#}$, and NOE$^{\#}$ parameters, two ROIs, enclosing the normal tissue and tumor, were analyzed. Tumor ROIs were drawn inside the border of the solid tumor mass based on the ADC and T$_2$w hyperintensities. Image contrast values were calculated using the signal intensity difference between tumor and normal regions. Data in graphs were presented as mean ± standard deviation. Statistical analysis was performed using the Student's t-test. The level of significance was considered at $p < 0.05$. All statistical analyses were performed using the statistical package SPSS (Version 18, Chicago, Illinois).

RESULTS

Simulation Results

Examples of simulated Z-spectra and MTR$_{asym}$ signals at the different relaxation delays (Td) and RF saturation lengths (Ts) are shown in Fig. 1. The initial longitudinal magnetization of water decreased with the shorter relaxation delay (steady-state M_z^w = 0.98

for Td = 8 s, and 0.87 for Td = 4 s), as shown in Fig. 1c–d. Thus, the MTR_{asym} (3.5ppm) effect on the bulk water signal was diminished with the shorter relaxation delay (MTR(3.5ppm)/MTR_{asym}(3.5ppm) = 0.724/0.04 for Td = 8 s, and 0.701/0.035 for Td = 4 s). In addition, the APTw effect was reduced at the shorter RF saturation length (MTR(3.5ppm)/MTR_{asym}(3.5ppm) = 0.701/0.036 for Ts = 2 s, and 0.801/0.016 for Ts = 0.5 s) due to the insufficient accumulation of the exchanged amide protons in the free bulk water proton pool, as shown in Fig. 1d–e.

Results from Monte Carlo simulations are shown in Fig. 2. The tumor contrast, standard deviation, and mean deviation maps contain 6×13 elements: rows increase from Td = 0.5 s to 6 s upwards and columns increase from Ts = 0.2 s to 6 s rightwards. The maximum values of standard deviation of MTR_{asym}(3.5ppm), $APT^{\#}$, and $NOE^{\#}$ signal contrast were 0.035, 0.034, and 0.035 %, respectively. The maximum values of mean deviation from the ground truth contrast map of MTR_{asym}(3.5ppm), $APT^{\#}$, and $NOE^{\#}$ were 0.0018, 0.0024, and 0.0029 %, respectively.

Figure 3 shows Bloch simulation results for the digital phantom with two compartments (C1 and C2 mimicked normal tissue and tumor, respectively). Based on a two-pool APT model, MTR_{asym}(3.5ppm) signals increased with the RF saturation length, regardless of the relaxation delay, when B_1 of 2.1 µT was applied. For a five-pool exchange model, however, MTR_{asym}(3.5ppm) signals in tumor showed a peak at Ts of 2 s and Td of 6 s (Fig. 3b), although the MTR_{asym}(3.5ppm) signal intensities of the tumor in the five-pool model were lower, in total, than those in the two-pool model due to upfield NOE signal contributions. Peaks in MTR_{asym}(3.5ppm) became more noticeable at a high RF saturation power level (~ 2.9 µT) as shown in Fig. 4a. In addition, both $APT^{\#}$ and $NOE^{\#}$ signals showed a trend similar to that of the two-pool MTR_{asym}(3.5ppm) signals, as shown in Fig. 3. Overall, MTR_{asym}(3.5ppm), $APT^{\#}$, and $NOE^{\#}$ tumor signals were higher at the relaxation delay of 6 s than 0.5 s, because the relaxation delay (or TR) was long enough compared to the water T_1 relaxation time.

Figure 4 shows MTR_{asym}(3.5ppm), $APT^{\#}$, and $NOE^{\#}$ signal features of tumor as a function of RF saturation length, with Td of 0.5 and 6 s, and B_1 of 0.5 and 2.9 µT. The MTR_{asym}(3.5ppm) signals were smaller at 0.5 µT than at 2.9 µT for relatively short RF saturation lengths. For long RF saturation lengths (> 3 s for Td = 0.5 s and 2 s for Td = 6 s), however, the MTR_{asym}(3.5ppm) became larger at 0.5 µT than at 2.9 µT, because of direct water saturation and semisolid MTC effects. Importantly, the MTR_{asym}(3.5ppm) signal intensities at a relatively high RF saturation power level (~ 2.9 µT) showed peaks at short RF saturation lengths (< 2 s) when a long relaxation delay (~ 6 s) was applied. The $APT^{\#}$ and $NOE^{\#}$ showed a trend similar to that shown in Fig. 4b–c.

Figure 5a shows MTR_{asym}(3.5ppm), $APT^{\#}$, and $NOE^{\#}$ contrast maps as a function of RF saturation length and relaxation delay with varied RF saturation powers. TRs were changed accordingly by each RF saturation or relaxation delay. The highest MTR_{asym}(3.5ppm) contrasts were observed at 1.3 µT for long RF saturation lengths (> 4 s) and relaxation delay (> 4 s). Overall, MTR_{asym}(3.5ppm) contrasts at relatively low RF saturation powers (< 1.3 µT) initially increased with the RF saturation length, but eventually reached a plateau in

particularly longer relaxation delays. Interestingly, the MTR_{asym}(3.5ppm) contrasts at relatively high RF saturation power levels (> 2.1 µT) showed peaks at short RF saturation lengths (< 2 s). The $APT^{\#}$ and $NOE^{\#}$ peaks shifted to longer RF saturation lengths relative to MTR_{asym}(3.5ppm) at higher RF saturation powers (> 2.1 µT). Negative $NOE^{\#}$ contrasts were observed at relatively low RF saturation powers (< 1.3 µT), as shown in Fig. 5a. As a result, the MTR_{asym}(3.5ppm) contrasts were higher than the $APT^{\#}$ contrasts at relatively low RF saturation powers (< 1.3 µT). However, the $APT^{\#}$ contrasts were slightly higher than the MTR_{asym}(3.5ppm) contrasts, because $NOE^{\#}$ contrasts became positive at higher RF saturation powers (> 2.1 µT) and longer RF saturation lengths (> 2 s). Contrasts were further normalized to TR for each metric (Fig. 5b). The normalized MTR_{asym}(3.5ppm), $APT^{\#}$, and $NOE^{\#}$ peaked to shorter RF saturation lengths and relaxation delays.

Figure 6 shows the influence of T_{1w} on MTR_{asym}(3.5ppm), $APT^{\#}$, and $NOE^{\#}$ at 3 T and 4.7 T. Three metrics showed negligible contrasts in the edema (C3) with respect to the tumor (C2) and normal tissues (C1) across all saturation power levels at clinical 3 T (Fig. 6b) while $APT^{\#}$ and $NOE^{\#}$ showed positive contrast in the edema at the relatively low RF saturation powers (<1.3 µT) at 4.7 T (Fig. 6c).

Experimental Results

Figure 7 shows experimentally acquired Z-spectra from tumor and normal brain regions with RF saturation powers of 1.3 and 2.1 µT, relaxation delays of 4 and 6 s, and RF saturation lengths of 0.4, 0.8, 1.2, 1.6, 2, and 4 s. As expected, the RF saturation power, RF saturation length, and relaxation delay dependencies were seen clearly due to the large effects from water spillover and semisolid MTC. Broad Z-spectra were observed at the higher RF saturation power levels and longer RF saturation lengths due to larger RF saturation widths and saturation effects. In addition, Z-spectra were largely reduced with decreasing relaxation delays.

The average MTR_{asym}(3.5ppm), $APT^{\#}$, and $NOE^{\#}$ signal intensities and contrasts of the tumor and normal tissues were compared in Fig. 8. Several important results could be observed: (i) The MTR_{asym}(3.5ppm) signal intensities of the normal tissue at two different RF saturation power levels were almost unchanged with different RF saturation lengths. The MTR_{asym}(3.5ppm) signal intensities of the normal tissue at 2.1 µT were almost zero due to a similar contribution of $APT^{\#}$ and $NOE^{\#}$ to the MTR_{asym}(3.5ppm) signals, while the MTR_{asym}(3.5ppm) signal intensities of the normal tissue at 1.3 µT were negative because of higher upfield $NOE^{\#}$ contributions. (ii) The MTR_{asym}(3.5ppm) of the tumor at 1.3 µT increased with the RF saturation length, while the MTR_{asym}(3.5ppm) of the tumor at 2.1 µT showed a peak at RF saturation lengths of 1.6 – 2 s, in line with the results of the Bloch simulation. The overall $APT^{\#}$ and $NOE^{\#}$ signal intensities of the tumor were higher at 1.3 µT than at 2.1 µT, while the MTR_{asym}(3.5ppm) signal intensities of the tumor were smaller at 1.3 µT than at 2.1 µT because of the different RF saturation powers and length dependencies of the $APT^{\#}$ and $NOE^{\#}$ signals, based on the fact that the NOE-related proton exchange rate is slower than the amide proton exchange rate (35, 51). (iii) Although overall $APT^{\#}$ and $NOE^{\#}$ contrasts increased with the RF saturation length, the MTR_{asym}(3.5ppm) contrast at 2.1 µT showed a peak at RF saturation length ranges of 1.6 to 2 s. However, the

MTR_{asym}(3.5ppm) contrast at 1.3 μT increased with the RF saturation length and reached a steady state. In addition, consistent with Figs. 5, the MTR_{asym}(3.5ppm) and $APT^{\#}$ contrasts were higher at 1.3 μT than at 2.1 μT. Notably, $NOE^{\#}$ contrasts became negligible or slightly positive at longer RF saturation lengths (> 3 s), resulting in $APT^{\#}$ contrasts that were higher than MTR_{asym}(3.5ppm) contrasts.

Figure 9 shows one example of the quantitative multi-parametric MRI maps for a representative tumor-bearing rat. The tumor was hyperintense on T_1^{obs}, T_2^{obs}, and ADC maps, compared to the normal brain region (also see Supporting Figs. S3). Consistent with Fig. 8, the MTR_{asym}(3.5ppm) signals at 1.3 μT increased with the RF saturation length, while the MTR_{asym}(3.5ppm) signals at 2.1 μT seemingly peaked at the RF saturation lengths of 1.6 – 2 s. In addition, overall MTR_{asym}(3.5ppm) contrasts were higher at 1.3 μT than at 2.1 μT. Note that color-bar scales for MTR_{asym}(3.5ppm) maps were adjusted to display an identical normal tissue background. The $APT^{\#}$ signals of the tumor at 1.3 μT increased with the RF saturation length, while the $APT^{\#}$ signals of the tumor at 2.1 μT seemingly reached a plateau after an RF saturation length of 1.6 s. Consistent with Fig. 8, overall $NOE^{\#}$ signals were lower at 2.1 μT than at 1.3 μT.

DISCUSSION

In this *in-vivo* APT tumor study, the optimization of APT imaging parameters, such as RF saturation power, RF saturation length, and relaxation delay, was crucial for the maximum APT signal intensity and contrast. Although many previous studies have been conducted on the optimization of pulse sequence design and saturation scheme, most of them were limited by the number of proton pools, CEST metrics, or combining parameters (40, 52–56). Here, we evaluated experimental parameters using five-pool Bloch equation-based simulations and an *in-vivo* rat tumor model at 4.7 T, a field strength that is close to clinical 3 T MRI scanners. We found that MTR_{asym}(3.5ppm) and $APT^{\#}$ contrasts increased with the RF saturation length and reached a steady-state at relatively low RF saturation powers (< 1.3 μT), while the maximum tumor contrast occurs with moderate RF saturation lengths (1.6 ~ 2 s) at relatively high RF saturation powers (> 2.1 μT). The peaks of MTR_{asym}(3.5ppm) and $APT^{\#}$ contrasts became more pronounced at higher RF saturation powers and longer relaxation delays (or longer TRs). In addition, MTR_{asym}(3.5ppm) contrasts were higher than $APT^{\#}$ contrasts at relatively low RF saturation powers (< 1.3 μT) and short RF saturation lengths (< 2 s) due to negative $NOE^{\#}$ contrasts (MTR_{asym}(3.5ppm) = $APT^{\#}$ – $NOE^{\#}$), while $NOE^{\#}$ contrasts became negligible or slightly positive at relatively high RF saturation powers (> 2.1 μT) and long RF saturation lengths (> 2 s), leading to higher $APT^{\#}$ contrasts relative to MTR_{asym}(3.5ppm) contrasts.

A higher RF saturation power caused substantial dilution effects by direct water saturation and semisolid MTC, reducing Z-spectra, even though it might provide more efficient saturation for water-exchangeable amide protons, based on Eq. [1] (37, 38). In addition, amide protons have a relatively higher optimal RF saturation power level than NOE-related protons, probably because the amide proton exchange rate is faster than the NOE-related proton exchange rate (29, 35). Therefore, the maximum MTR_{asym}(3.5ppm) contrast can be determined through balancing the direct water saturation effect, the semisolid MTC effect,

the RF saturation efficiency, and the different RF power dependencies of the downfield APT and upfield NOE signals. In our Bloch equation-based simulations and *in-vivo* tumor studies, maximum $MTR_{asym}(3.5ppm)$ (for Ts > 1.6 s) and $APT^{\#}$ (for Ts > 2 s) contrasts were observed at the intermediate RF saturation power (≈ 1.3 μT). Nevertheless, rather than using a saturation power of 1.3 μT, a power of 2 μT is currently being used for tumor patients on clinical 3 T scanners, because it leads to a positive $MTR_{asym}(3.5ppm)$ signal intensity in brain tumors while the tumor periphery (e.g., peritumoral edema areas) and the surrounding normal-appearing white matter are almost nulled. At a saturation power of 1.3 μT, however, the negative $MTR_{asym}(3.5ppm)$ signal intensity of the normal tissue may complicate the interpretation of the images, because the $MTR_{asym}(3.5ppm)$ signal intensity of the cerebrospinal fluid (CSF) is almost zero, which seems comparable to that of the tumor ($MTR_{asym}(3.5ppm)$: normal < tumor $\approx$ CSF) (53).

We observed that a relaxation delay influences the Z-spectrum by alteration of the magnitude of the longitudinal magnetization of water. Long TRs or relaxation delays raised the Z-spectra and led to an increase in water signal reduction, further enhancing the APT effect, in line with previous theoretical studies (40, 54). However, no significant differences were observed in $MTR_{asym}(3.5ppm)$, $APT^{\#}$, and $NOE^{\#}$ signals with a relaxation delay of 4 s and 6 s (Fig. 8) in the *in vivo* study. Presumably, the relaxation delays might be long enough, compared to water T_1 relaxation time (normal/tumor = 1.53/1.95 s). A long (several seconds) RF saturation pulse allows more accumulation of saturated protons in the free water pool and maintains a steady-state saturation (56). However, the effect of the RF saturation length had an influence on the Z-spectrum similar to that of the RF saturation power, in which dilution effects by direct water saturation and semisolid MTC increased with the RF saturation length (Fig. 7). Consequently, an extensive dilution effect, caused by longer (> 2 s) saturations and higher RF saturation powers (> 2.1 μT), instead reduces the $MTR_{asym}(3.5ppm)$ contrast, which is consistent with our Bloch simulation results. In the *in-vivo* study, we observed the maximum $MTR_{asym}(3.5ppm)$ contrasts at intermediate RF saturation lengths (1.6 ~ 2 s) under the relatively low RF saturation power of 1.3 μT.

We observed a nonlinear relationship between the CEST metric signals and water T_1 relaxation time as shown in Fig. 6. Particularly, no contrasts between edema ($T_1 = 1.4$ s) and normal ($T_1 = 1.2$ s) tissues were visually observed at a magnetic field strength of 3 T, in line with previous observations from tumor patient and simulation studies (22, 37, 57). Moreover, an increased water T_1 effect could be mostly compensated by an elevated water content in peritumoral edema and tumor core regions. At a magnetic field strength of 4.7 T, minor contrasts between edema ($T_1 = 1.95$ s) and normal ($T_1 = 1.53$ s) tissues can be seen, which were decreased with the RF saturation power level and became negligible (> 2.1 μT) probably due to water direct saturation and semisolid MTC effects, as reported before (37, 43).

Numerous previous *in vivo* studies at 4.7 T from us and other investigators (34, 35, 58–61) have used a CW-based long saturation length (> 3 s) to reach steady-state CEST signals. Further, a long TR or Td is helpful for the water magnetization to fully recover to the equilibrium, which would thus result in the high CEST effect. In this study, to understand the CEST effect for a range of Td values, our simulations used several Td values between

0.5 and 8 s. Fortunately, the use of shorter relaxation delays and saturation lengths could be efficient in $MTR_{asym}(3.5ppm)$ and $APT^{\#}$ tumor contrasts, as shown in Fig. 5b, which help guide optimization of APT imaging. However, it should be noted that water T_1 relaxation effects overwhelm chemical exchange saturation effects when a very short relaxation delay was used, as shown in Fig. 10. The water longitudinal magnetization still grows in spite of the presence of the off-resonance RF irradiation, particularly at low RF saturation powers (black and red lines in Fig. 10a). Thus, the use of a very short TR or Td for reducing acquisition time causes an inefficient RF saturation scheme.

CONCLUSIONS

$MTR_{asym}(3.5ppm)$ images are not clean in terms of only a single component, because the standard MTR asymmetry analysis combines the information from upfield NOE signals. However, the potential confounding effect of NOEs was found to actually be symbiotic with APT in the detection of tumors when a lower RF saturation power than ~2 µT is applied, although $NOE^{\#}$ tumor contrasts were relatively small. In order to obtain the maximum $MTR_{asym}(3.5ppm)$ and $APT^{\#}$ tumor contrast, a relatively lower RF saturation power with a relatively longer RF saturation length (several seconds) is required (a set-up used currently in most animal studies). For time-efficient manner, however, $MTR_{asym}(3.5ppm)$ and $APT^{\#}$ contrast could be maximized at intermediate relaxation delays and saturation lengths.

Supplementary Material

Refer to Web version on PubMed Central for supplementary material.

Acknowledgments

References

1. Ward KM, Aletras AH, Balaban RS. A new class of contrast agents for MRI based on proton chemical exchange dependent saturation transfer (CEST). J Magn Reson. 2000; 143:79–87. [PubMed: 10698648]

2. Zhou J, van Zijl PC. Chemical exchange saturation transfer imaging and spectroscopy. Progr NMR Spectr. 2006; 48:109–136.

3. van Zijl PCM, Yadav NN. Chemical exchange saturation transfer (CEST): What is in a name and what isn't? Magn Reson Med. 2011; 65:927–948. [PubMed: 21337419]

4. Vinogradov E, Sherry AD, Lenkinski RE. CEST: From basic principles to applications, challenges and opportunities. J Magn Reson. 2013; 229:155–172. [PubMed: 23273841]

5. Zhou J, Payen J, Wilson DA, Traystman RJ, van Zijl PCM. Using the amide proton signals of intracellular proteins and peptides to detect pH effects in MRI. Nature Med. 2003; 9:1085–1090. [PubMed: 12872167]

6. Zhou J, Lal B, Wilson DA, Laterra J, van Zijl PCM. Amide proton transfer (APT) contrast for imaging of brain tumors. Magn Reson Med. 2003; 50:1120–1126. [PubMed: 14648559]

7. Tietze A, Blicher J, Mikkelsen IK, Ostergaard L, Strother MK, Smith SA, Donahue MJ. Assessment of ischemic penumbra in patients with hyperacute stroke using amide proton transfer (APT) chemical exchange saturation transfer (CEST) MRI. NMR Biomed. 2014; 27:163–174. [PubMed: 24288260]

8. Harston GW, Tee YK, Blockley N, Okell TW, Thandeswaran S, Shaya G, Sheerin F, Cellerini M, Payne S, Jezzard P, Chappell M, Kennedy J. Identifying the ischaemic penumbra using pH-weighted magnetic resonance imaging. Brain. 2015; 138:36–42. [PubMed: 25564491]

9. Heo HY, Zhang Y, Burton TM, Jiang S, Zhao Y, van Zijl PCM, Leigh R, Zhou J. Improving the detection sensitivity of pH-weighted amide proton transfer MRI in acute stroke patients using extrapolated semisolid magnetization transfer reference signals. Magn Reson Med. 2017; 78:871–880. [PubMed: 28639301]

10. Zhou JY, van Zijl PCM. Defining an acidosis-based ischemic penumbra from pH-weighted MRI. Transl Stroke Res. 2012; 3:76–83.

11. Zhou J, Blakeley JO, Hua J, Kim M, Laterra J, Pomper MG, van Zijl PCM. Practical data acquisition method for human brain tumor amide proton transfer (APT) imaging. Magn Reson Med. 2008; 60:842–849. [PubMed: 18816868]

12. Sakata A, Okada T, Yamamoto A, Kanagaki M, Fushimi Y, Dodo T, Arakawa Y, Schmitt B, Miyamoto S, Togashi K. Grading glial tumors with amide proton transfer MR imaging: different analytical approaches. J Neuro-Onc. 2015; 122:339–348.

13. Jiang S, Yu H, Wang X, Lu S, Li Y, Feng L, Zhang Y, Heo HY, Lee DH, Zhou J, Wen Z. Molecular MRI differentiation between primary central nervous system lymphomas and high-grade gliomas using endogenous protein-based amide proton transfer MR imaging at 3 Tesla. Eur Radiol. 2016; 26:64–71. [PubMed: 25925361]

14. Jiang S, Eberhart CG, Zhang Y, Heo H-Y, Wen Z, Blair L, Qin H, Lim M, Quinones-Hinojosa A, Weingart JD, Barker PB, Pomper MG, Laterra J, van Zijl PCM, Blakeley JO, Zhou J. Amide proton transfer-weighted MR image-guided stereotactic biopsy in patients with newly diagnosed gliomas. Eur J Cancer. 2017; 83:9–18. [PubMed: 28704644]

15. Choi YS, Ahn SS, Lee SK, Chang JH, Kang SG, Kim SH, Zhou J. Amide proton transfer imaging to discriminate between low- and high-grade gliomas: added value to apparent diffusion coefficient and relative cerebral blood volume. Eur Radiol. 2017; 27:3181–3189. [PubMed: 28116517]

16. Heo HY, Zhang Y, Lee DH, Jiang S, Zhao X, Zhou J. Accelerating chemical exchange saturation transfer (CEST) MRI by combining compressed sensing and sensitivity encoding techniques. Magn Reson Med. 2017; 77:779–786. [PubMed: 26888295]

17. Jia G, Abaza R, Williams JD, Zynger DL, Zhou JY, Shah ZK, Patel M, Sammet S, Wei L, Bahnson RR, Knopp MV. Amide proton transfer MR imaging of prostate cancer: A preliminary study. J Magn Reson Imaging. 2011; 33:647–654. [PubMed: 21563248]

18. Yuan J, Chen S, King AD, Zhou J, Bhatia KS, Zhang Q, Yeung DK, Wei J, Mok GS, Wang YX. Amide proton transfer-weighted imaging of the head and neck at 3 T: a feasibility study on healthy human subjects and patients with head and neck cancer. NMR Biomed. 2014; 27:1239–1247. [PubMed: 25137521]

19. Li C, Peng S, Wang R, Chen H, Su W, Zhao X, Zhou J, Chen M. Chemical exchange saturation transfer MR imaging of Parkinson's disease at 3 Tesla. Eur Radiol. 2014; 24:2631–2639. [PubMed: 25038850]

20. Jeong HK, Han K, Zhou J, Zhao Y, Choi YS, Lee SK, Ahn SS. Characterizing amide proton transfer imaging in haemorrhage brain lesions using 3T MRI. Eur Radiol. 2017; 27:1577–1584. [PubMed: 27380905]

21. Zhang H, Kang H, Zhao X, Jiang S, Zhang Y, Zhou J, Peng Y. Amide proton transfer (APT) MR imaging and magnetization transfer (MT) MR imaging of pediatric brain development. Eur Radiol. 2016; 26:3368–3376. [PubMed: 26762941]

22. Zhou J, Zhu H, Lim M, Blair L, Quinones-Hinojosa A, Messina AA, Eberhart CG, Pomper MG, Laterra J, Barker PB, van Zijl PCM, Blakeley JO. Three-dimensional amide proton transfer MR imaging of gliomas: Initial experience and comparison with gadolinium enhancement. J Magn Reson Imaging. 2013; 38:1119–1128. [PubMed: 23440878]

23. Togao O, Yoshiura T, Keupp J, Hiwatashi A, Yamashita K, Kikuchi K, Suzuki Y, Suzuki SO, Iwaki T, Hata N, Mizoguchi M, Yoshimoto K, Sagiyama K, Takahashi M, Honda H. Amide proton transfer imaging of adult diffuse gliomas: correlation with histopathological grades. Neuro Oncol. 2014; 16:441–448. [PubMed: 24305718]

24. Ma B, Blakeley JO, Hong X, Zhang H, Jiang S, Blair L, Zhang Y, Heo HY, Zhang M, van Zijl PC, Zhou J. Applying amide proton transfer-weighted MRI to distinguish pseudoprogression from true progression in malignant gliomas. J Magn Reson Imaging. 2016; 44:456–462. [PubMed: 26788865]

25. Jiang S, Zou T, Eberhart CG, Villalobos MAV, Heo HY, Zhang Y, Wang Y, Wang X, Yu H, Du Y, van Zijl PCM, Wen Z, Zhou J. Predicting IDH mutation status in grade II gliomas using amide proton transfer-weighted (APTw) MRI. Magn Reson Med. 2017; 78:1100–1109. [PubMed: 28714279]

26. Jiang S, Rui Q, Wang Y, Heo HY, Zou T, Yu H, Zhang Y, Wang X, Du Y, Wen X, Chen F, Wang J, Eberhart CG, Zhou J, Wen Z. Discriminating MGMT promoter methylation status in patients with glioblastoma employing amide proton transfer-weighted MRI metrics. Eur Radiol. 2017; doi: 10.1007/s00330-00017-05182-00334

27. Ling W, Regatte RR, Navon G, Jerschow A. Assessment of glycosaminoglycan concentration in vivo by chemical exchange-dependent saturation transfer (gagCEST). Proc Natl Acad Sci (USA). 2008; 105:2266–2270. [PubMed: 18268341]

28. Jones CK, Huang A, Xu J, Edden RA, Schar M, Hua J, Oskolkov N, Zaca D, Zhou J, McMahon MT, Pillai JJ, van Zijl PC. Nuclear Overhauser enhancement (NOE) imaging in the human brain at 7T. Neuroimage. 2013; 77:114–124. [PubMed: 23567889]

29. Jin T, Wang P, Zong XP, Kim SG. MR imaging of the amide-proton transfer effect and the pH-insensitive nuclear overhauser effect at 9.4 T. Magnet Reson Med. 2013; 69:760–770.

30. Liu D, Zhou J, Xue R, Zuo Z, An J, Wang DJJ. Quantitative characterization of nuclear Overhauser enhancement and amide proton transfer effects in the human brain at 7 Tesla. Magn Reson Med. 2013; 70:1070–1081. [PubMed: 23238951]

31. Paech D, Zaiss M, Meissner JE, Windschuh J, Wiestler B, Bachert P, Neumann JO, Kickingereder P, Schlemmer HP, Wick W, Nagel AM, Heiland S, Ladd ME, Bendszus M, Radbruch A. Nuclear Overhauser enhancement mediated chemical exchange saturation transfer imaging at 7 Tesla in glioblastoma patients. PLoS One. 2014; 9:e104181. [PubMed: 25111650]

32. Lu J, Zhou J, Cai C, Cai S, Chen Z. Observation of true and pseudo NOE signals using CEST-MRI and CEST-MRS sequences with and without lipid suppression. Magn Reson Med. 2015; 73:1615–1622. [PubMed: 24803172]

33. Heo HY, Jones CK, Hua J, Yadav N, Agarwal S, Zhou J, van Zijl PC, Pillai JJ. Whole-brain amide proton transfer (APT) and nuclear overhauser enhancement (NOE) imaging in glioma patients using low-power steady-state pulsed chemical exchange saturation transfer (CEST) imaging at 7T. J Magn Reson Imaging. 2016; 44:41–50. [PubMed: 26663561]

34. Zhou J, Hong X, Zhao X, Gao J-H, Yuan J. APT-weighted and NOE-weighted image contrasts in glioma with different RF saturation powers based on magnetization transfer ratio asymmetry analyses. Magn Reson Med. 2013; 70:320–327. [PubMed: 23661598]

35. Heo HY, Zhang Y, Lee DH, Hong X, Zhou J. Quantitative assessment of amide proton transfer (APT) and nuclear overhauser enhancement (NOE) imaging with extrapolated semi-solid magnetization transfer reference (EMR) signals: Application to a rat glioma model at 4.7 tesla. Magn Reson Med. 2016; 75:137–149. [PubMed: 25753614]

36. Heo HY, Zhang Y, Jiang S, Lee DH, Zhou J. Quantitative assessment of amide proton transfer (APT) and nuclear overhauser enhancement (NOE) imaging with extrapolated semisolid magnetization transfer reference (EMR) signals: II. Comparison of three EMR models and application to human brain glioma at 3 Tesla. Magn Reson Med. 2016; 75:1630–1639. [PubMed: 26033553]

37. Heo HY, Lee DH, Zhang Y, Zhao X, Jiang S, Chen M, Zhou J. Insight into the quantitative metrics of chemical exchange saturation transfer (CEST) imaging. Magn Reson Med. 2017; 77:1853–1865. [PubMed: 27170222]

38. Zhou J, Wilson DA, Sun PZ, Klaus JA, van Zijl PCM. Quantitative description of proton exchange processes between water and endogenous and exogenous agents for WEX, CEST, and APT experiments. Magn Reson Med. 2004; 51:945–952. [PubMed: 15122676]

39. Zaiss M, Xu J, Goerke S, Khan IS, Singer RJ, Gore JC, Gochberg DF, Bachert P. Inverse Z-spectrum analysis for spillover-, MT-, and T1 -corrected steady-state pulsed CEST-MRI -

application to pH-weighted MRI of acute stroke. NMR Biomed. 2014; 27:240–252. [PubMed: 24395553]

40. Sun PZ, Lu J, Wu Y, Xiao G, Wu R. Evaluation of the dependence of CEST-EPI measurement on repetition time, RF irradiation duty cycle and imaging flip angle for enhanced pH sensitivity. Phys Med Biol. 2013; 58:N229–240. [PubMed: 23939228]

41. Woessner DE, Zhang S, Merritt ME, Sherry AD. Numerical solution of the Bloch equations provides insights into the optimum design of PARACEST agents for MRI. Magn Reson Med. 2005; 53:790–799. [PubMed: 15799055]

42. Chappell MA, Donahue MJ, Tee YK, Khrapitchev AA, Sibson NR, Jezzard P, Payne SJ. Quantitative Bayesian model-based analysis of amide proton transfer MRI. Magn Reson Med. 2013; 70:556–567. [PubMed: 23008121]

43. Lee DH, Heo HY, Zhang K, Zhang Y, Jiang S, Zhao X, Zhou J. Quantitative assessment of the effects of water proton concentration and water T1 changes on amide proton transfer (APT) and nuclear overhauser enhancement (NOE) MRI: The origin of the APT imaging signal in brain tumor. Magn Reson Med. 2017; 77:855–863. [PubMed: 26841096]

44. Manton DJ, Lowry M, Blackband SJ, Horsman A. Determination of proton metabolite concentrations and relaxation parameters in normal human brain and intracranial tumours. NMR Biomed. 1995; 8:104–112. [PubMed: 8579997]

45. Henkelman RM. Measurement of signal intensities in the presence of noise in MR images. Med Phys. 1985; 12:232–233. [PubMed: 4000083]

46. Kim M, Gillen J, Landman BA, Zhou J, van Zijl PC. Water saturation shift referencing (WASSR) for chemical exchange saturation transfer (CEST) experiments. Magn Reson Med. 2009; 61:1441–1450. [PubMed: 19358232]

47. Quesson B, Thiaudiere E, Delalande C, Chateil JF, Moonen CT, Canioni P. Magnetization transfer imaging of rat brain under non-steady-state conditions. Contrast prediction using a binary spin-bath model and a super-lorentzian lineshape. J Magn Reson. 1998; 130:321–328. [PubMed: 9500906]

48. Henkelman RM, Huang X, Xiang Q-S, Stanisz GJ, Swanson SD, Bronskill MJ. Quantitative interpretation of magnetization transfer. Magn Reson Med. 1993; 1993:759–766.

49. Desmond KL, Stanisz GJ. Understanding quantitative pulsed CEST in the presence of MT. Magn Reson Med. 2012; 67:979–990. [PubMed: 21858864]

50. Ethofer T, Mader I, Seeger U, Helms G, Erb M, Grodd W, Ludolph A, Klose U. Comparison of longitudinal metabolite relaxation times in different regions of the human brain at 1.5 and 3 Tesla. Magn Reson Med. 2003; 50:1296–1301. [PubMed: 14648578]

51. Xu J, Yadav NN, Bar-Shir A, Jones CK, Chan KW, Zhang J, Walczak P, McMahon MT, van Zijl PC. Variable delay multi-pulse train for fast chemical exchange saturation transfer and relayed-nuclear overhauser enhancement MRI. Magn Reson Med. 2014; 71:1798–1812. [PubMed: 23813483]

52. Sun PZ, Wang E, Cheung JS, Zhang X, Benner T, Sorensen AG. Simulation and optimization of pulsed radio frequency irradiation scheme for chemical exchange saturation transfer (CEST) MRI-demonstration of pH-weighted pulsed-amide proton CEST MRI in an animal model of acute cerebral ischemia. Magn Reson Med. 2011; 66:1042–1048. [PubMed: 21437977]

53. Zhao X, Wen Z, Huang F, Lu S, Wang X, Hu S, Zu D, Zhou J. Saturation power dependence of amide proton transfer image contrasts in human brain tumors and strokes at 3 T. Magn Reson Med. 2011; 66:1033–1041. [PubMed: 21394783]

54. Xiao G, Sun PZ, Wu R. Fast simulation and optimization of pulse-train chemical exchange saturation transfer (CEST) imaging. Phys Med Biol. 2015; 60:4719–4730. [PubMed: 26020414]

55. Wada T, Togao O, Tokunaga C, Funatsu R, Kobayashi K, Nakamura Y. Effect of the saturation pulse duration on chemical exchange saturation transfer in amide proton transfer MR imaging: a phantom study. Radiol Phys Technol. 2016; 9:15–21. [PubMed: 26099607]

56. Togao O, Hiwatashi A, Keupp J, Yamashita K, Kikuchi K, Yoshiura T, Yoneyama M, Kruiskamp MJ, Sagiyama K, Takahashi M, Honda H. Amide Proton Transfer Imaging of Diffuse Gliomas: Effect of Saturation Pulse Length in Parallel Transmission-Based Technique. PLoS One. 2016; 11doi: 10.1371/journal.pone.0155925

57. Wen Z, Hu S, Huang F, Wang X, Guo L, Quan X, Wang S, Zhou J. MR imaging of high-grade brain tumors using endogenous protein and peptide-based contrast. Neuroimage. 2010; 51:616–622. [PubMed: 20188197]

58. Yuwen Zhou I, Wang E, Cheung JS, Lu D, Ji Y, Zhang X, Fulci G, Sun PZ. Direct saturation-corrected chemical exchange saturation transfer MRI of glioma: Simplified decoupling of amide proton transfer and nuclear overhauser effect contrasts. Magn Reson Med. 2017; 78:2307–2314. [PubMed: 29030880]

59. Huang SM, Jan ML, Liang HC, Chang CH, Wu YC, Tsai SY, Wang FN. Investigation of Readout RF Pulse Impact on the Chemical Exchange Saturation Transfer Spectrum. Sci Rep. 2015; 5:15062. [PubMed: 26455576]

60. Zhou IY, Wang E, Cheung JS, Zhang X, Fulci G, Sun PZ. Quantitative chemical exchange saturation transfer (CEST) MRI of glioma using Image Downsampling Expedited Adaptive Least-squares (IDEAL) fitting. Sci Rep. 2017; 7:84. [PubMed: 28273886]

61. Lu J, Zhou J, Cai C, Cai S, Chen Z. Observation of true and pseudo NOE signals using CEST-MRI and CEST-MRS sequences with and without lipid suppression. Magn Reson Med. 2015; 73:1615–1622. [PubMed: 24803172]
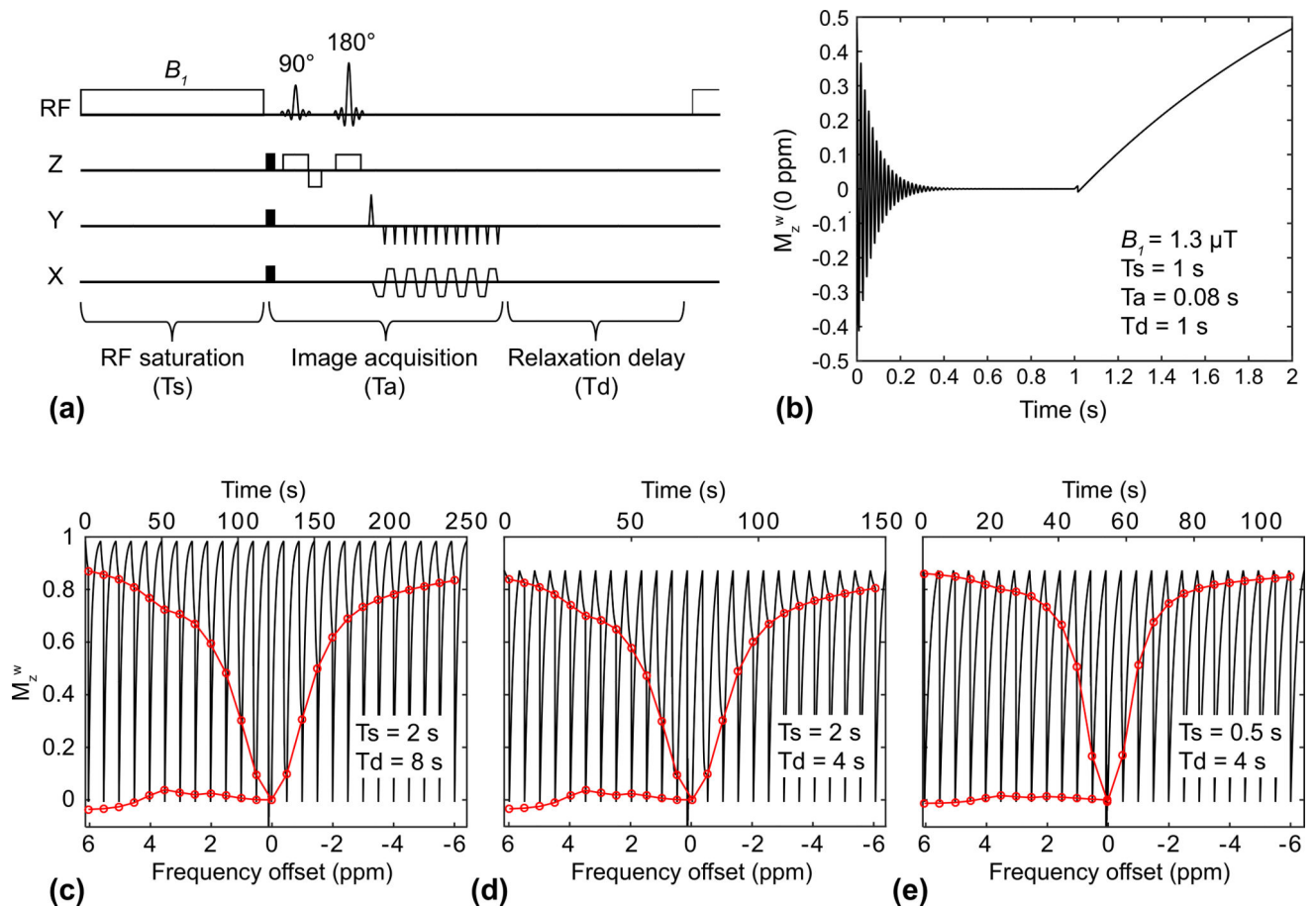
Figure 1.
Effects of RF saturation length (Ts) and relaxation delay (Td) on APT signal intensities, as measured by MTR asymmetry. (a) Illustration of the spin-echo-based CEST sequence with a single-shot EPI readout. Single TR consists of RF saturation, image acquisition (Ta), and relaxation delay time parts. (b) The evolution of the longitudinal magnetization of the water (M_z^w) at 0 ppm during a continuous RF saturation pulse, 90°, 180° RF pulses, and T_1 relaxation recovery. (c–e) The evolution of M_z^w during an RF saturation frequency sweep (−6 ~ 6 ppm at intervals of 0.5 ppm and B_1 of 1.3 μT) with different Ts and Td times. Red lines indicate corresponding Z-spectra and MTR_{asym}. These simulations are based on a five-pool exchange model at a B_0 magnetic field strength of 4.7 T and on a tumor case given in Methods.
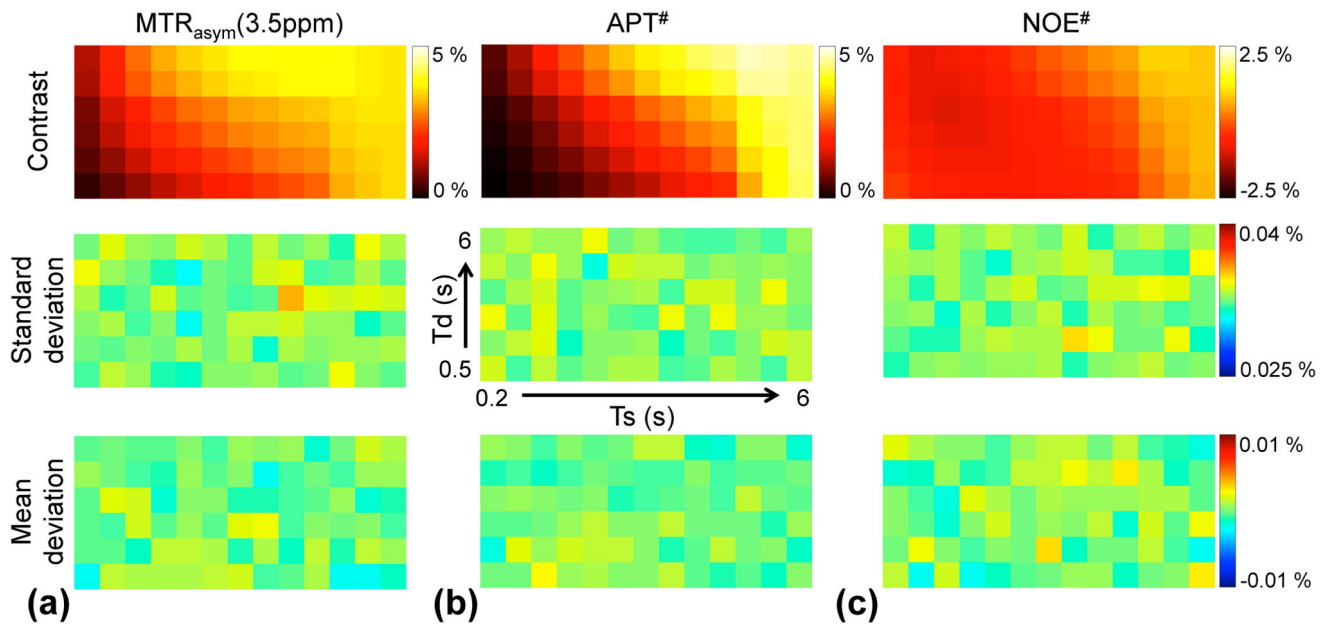
Figure 2.
Monte Carlo simulation results (1,000 trials) at a RF saturation power of 2.1 μT and magnetic field strength of 4.7 T. Tumor contrast, standard deviation, and mean deviation maps of (a) MTR_{asym}(3.5ppm), (b) $APT^{\#}$, and (c) $NOE^{\#}$. In each map, columns increase from Ts = 0.2 s to 6 s rightwards and rows increase from Td = 0.5 s to 6 s upwards.
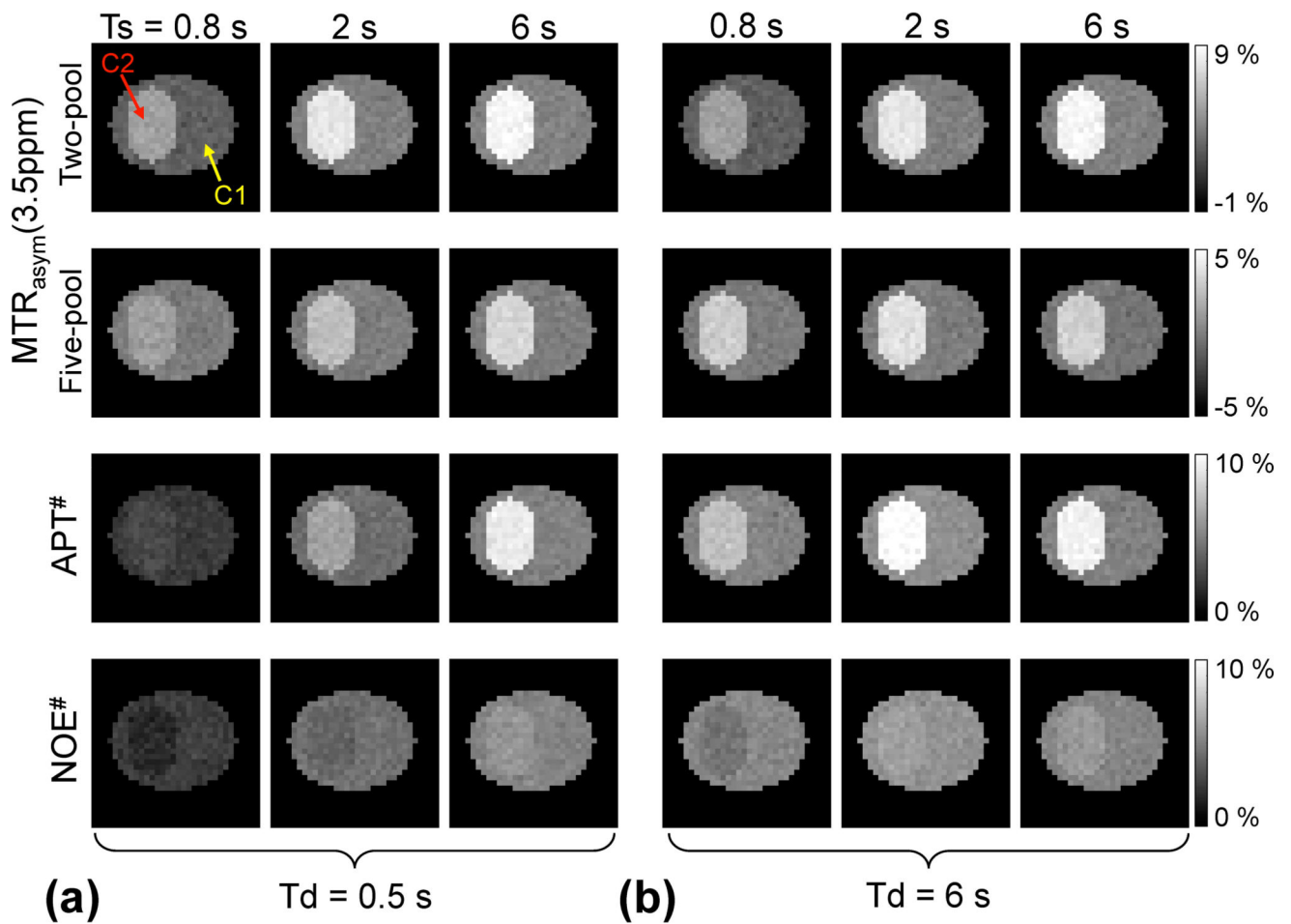
Figure 3.
MTR$_{asym}$(3.5ppm) obtained from a two-pool APT exchange model and a five-pool exchange model, APT$^{\#}$, and NOE$^{\#}$ signal features as a function of RF saturation length at relaxation delays of (a) 0.5 s and (b) 6 s under a RF saturation power of 2.1 μT and magnetic field strength of 4.7 T. Two homogenous compartments (C1 and C2) in digital phantoms mimic normal and tumor tissues, respectively.
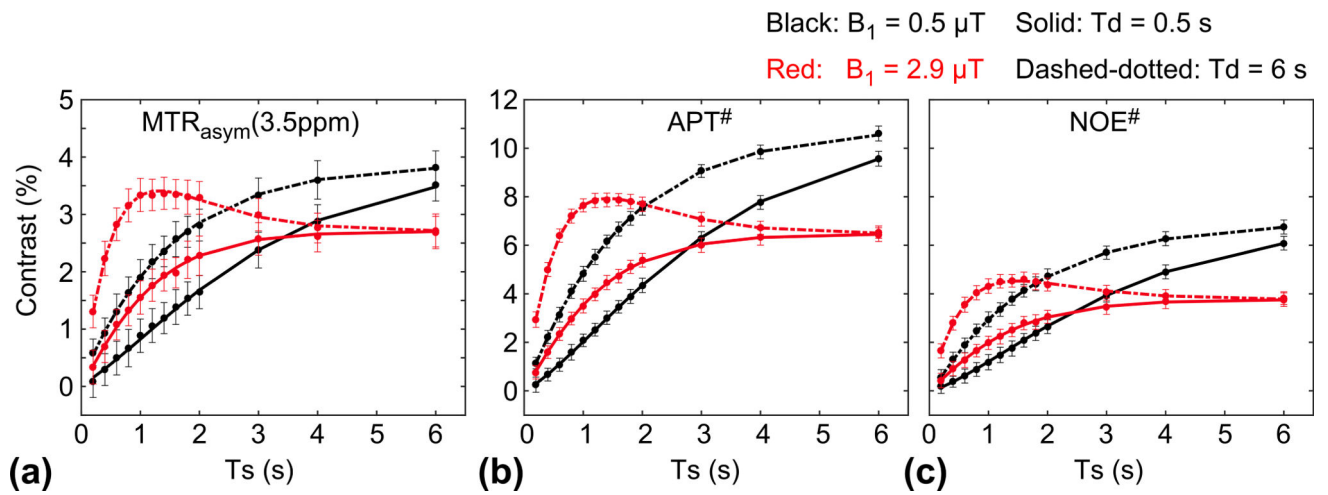
Figure 4.
MTR$_{asym}$(3.5ppm), APT$^{\#}$, and NOE$^{\#}$ signal contrast (= tumor − normal) as a function of RF saturation length at two RF saturation power levels (B$_1$ = 0.5 and 2.9 µT) and relaxation delays (Td = 0.5, and 6 s). (a) MTR$_{asym}$(3.5ppm), (b) APT$^{\#}$, (c) NOE$^{\#}$ signal contrast.
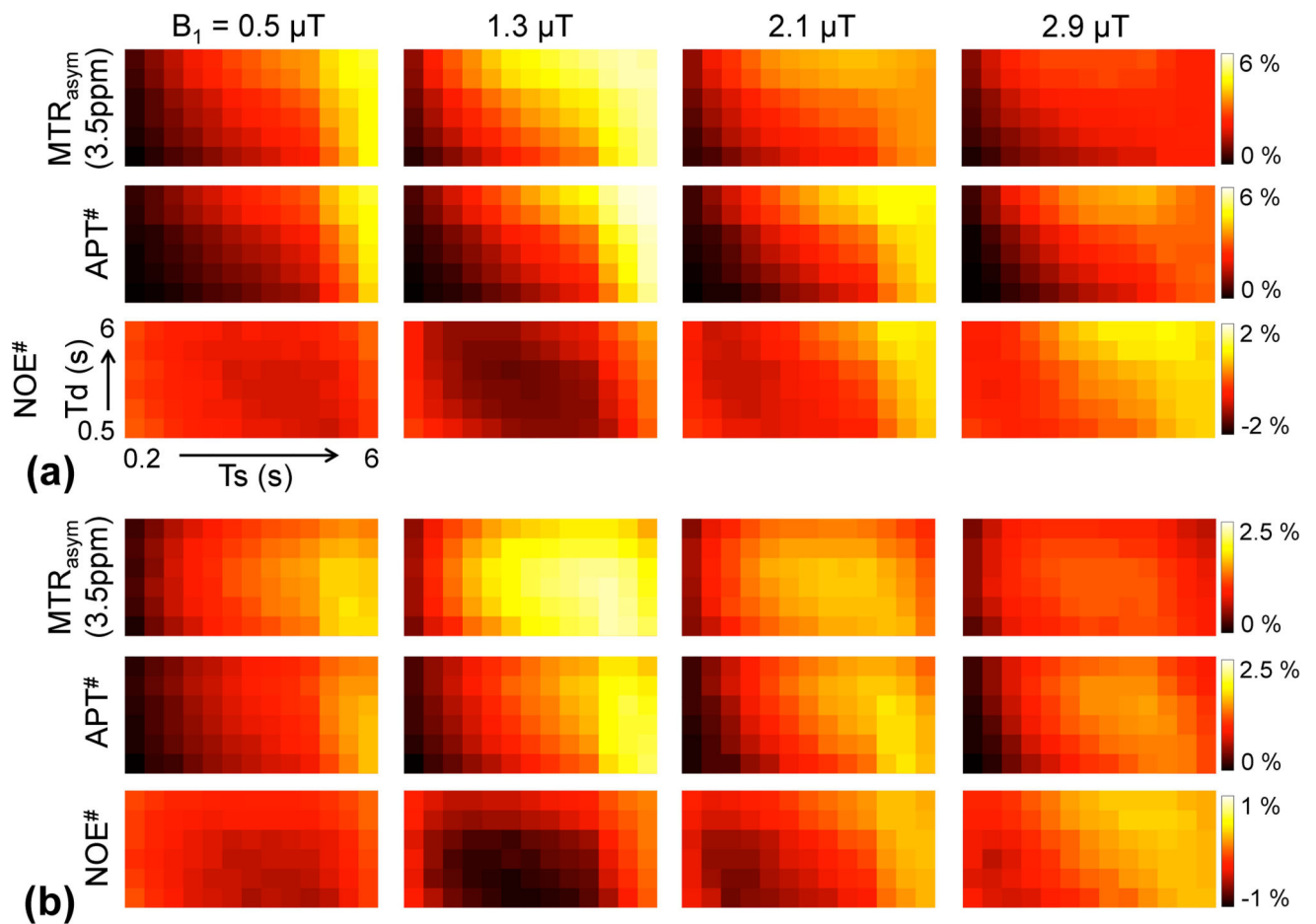
Figure 5.
(a) MTR$_{asym}$(3.5ppm), APT$^{\#}$, and NOE$^{\#}$ signal contrast maps (= tumor – normal) and (b) normalized MTR$_{asym}$(3.5ppm), APT$^{\#}$, and NOE$^{\#}$ signal contrast maps (normalized by TR) as a function of RF saturation length and relaxation delay at various RF saturation power levels (B$_1$ = 0.5, 1.3, 2.1, and 2.9 μT). In each map, columns increase from Ts = 0.2 s to 6 s rightwards and rows increase from Td = 0.5 s to 6 s upwards.
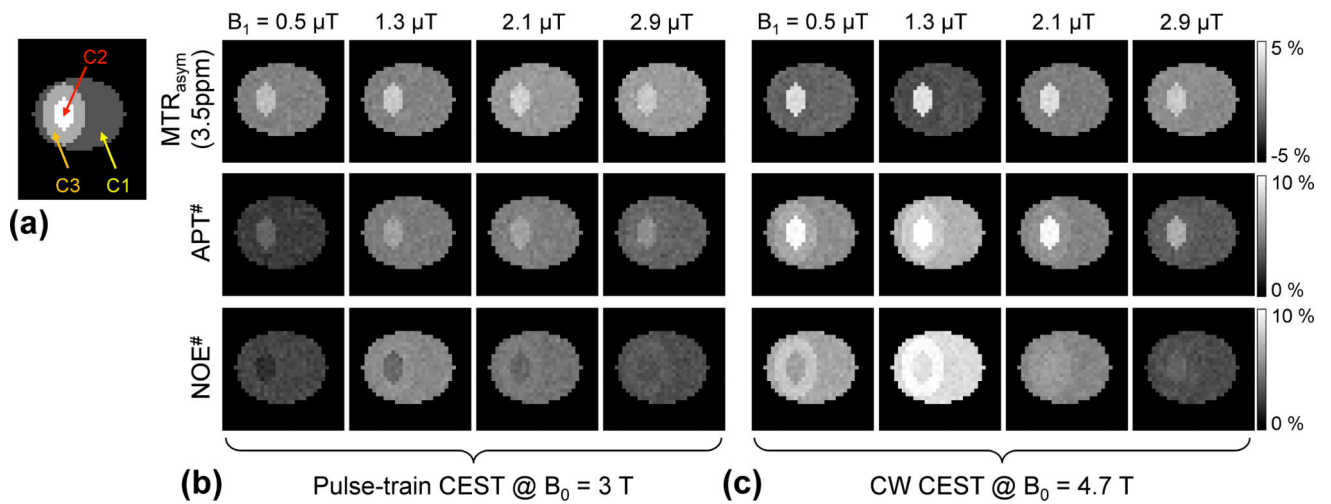
Figure 6.
Water T_1 relaxation effects on MTR_{asym}(3.5ppm), $APT^\#$, and $NOE^\#$ contrast. (a) Three compartments mimic normal (C1), tumor (C2), and edema (C3) tissues, respectively. The water relaxation parameters (T_{1w} and T_{2w}) of edema are same as for tumor case; but other parameters are identical to those used in the normal case. MTR_{asym}(3.5ppm), $APT^\#$, and $NOE^\#$ maps at (b) clinical 3 T, and (c) 4.7 T field strengths.
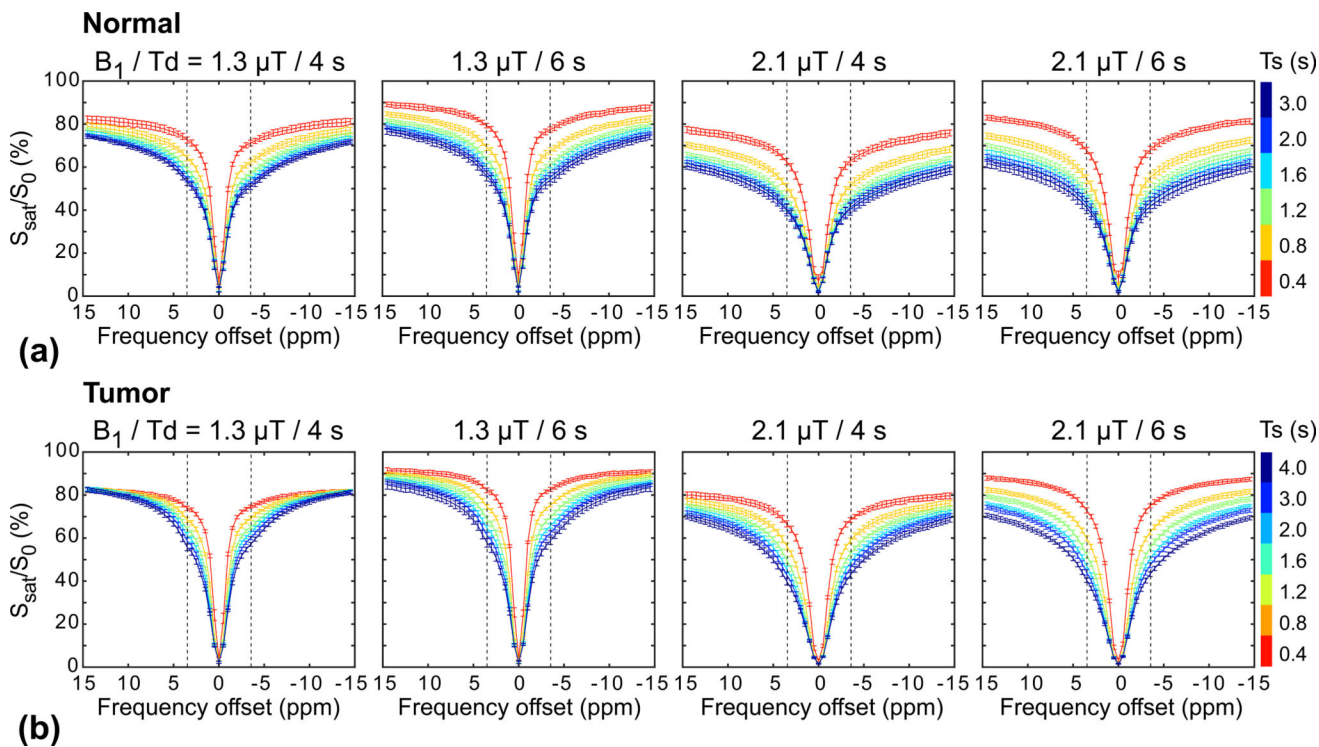
Normal

(a)

Tumor

(b)

Figure 7.
Average experimental Z-spectra (n = 6) for the normal brain (a) and tumor (b) regions at RF saturation power levels (1.3 and 2.1 μT), relaxation delays (4 and 6 s), and RF saturation lengths (0.4, 0.8, 1.2, 1.6, 2, and 4 s). The left and right vertical dashed lines represent the frequency offsets of 3.5 ppm and −3.5 ppm, respectively.
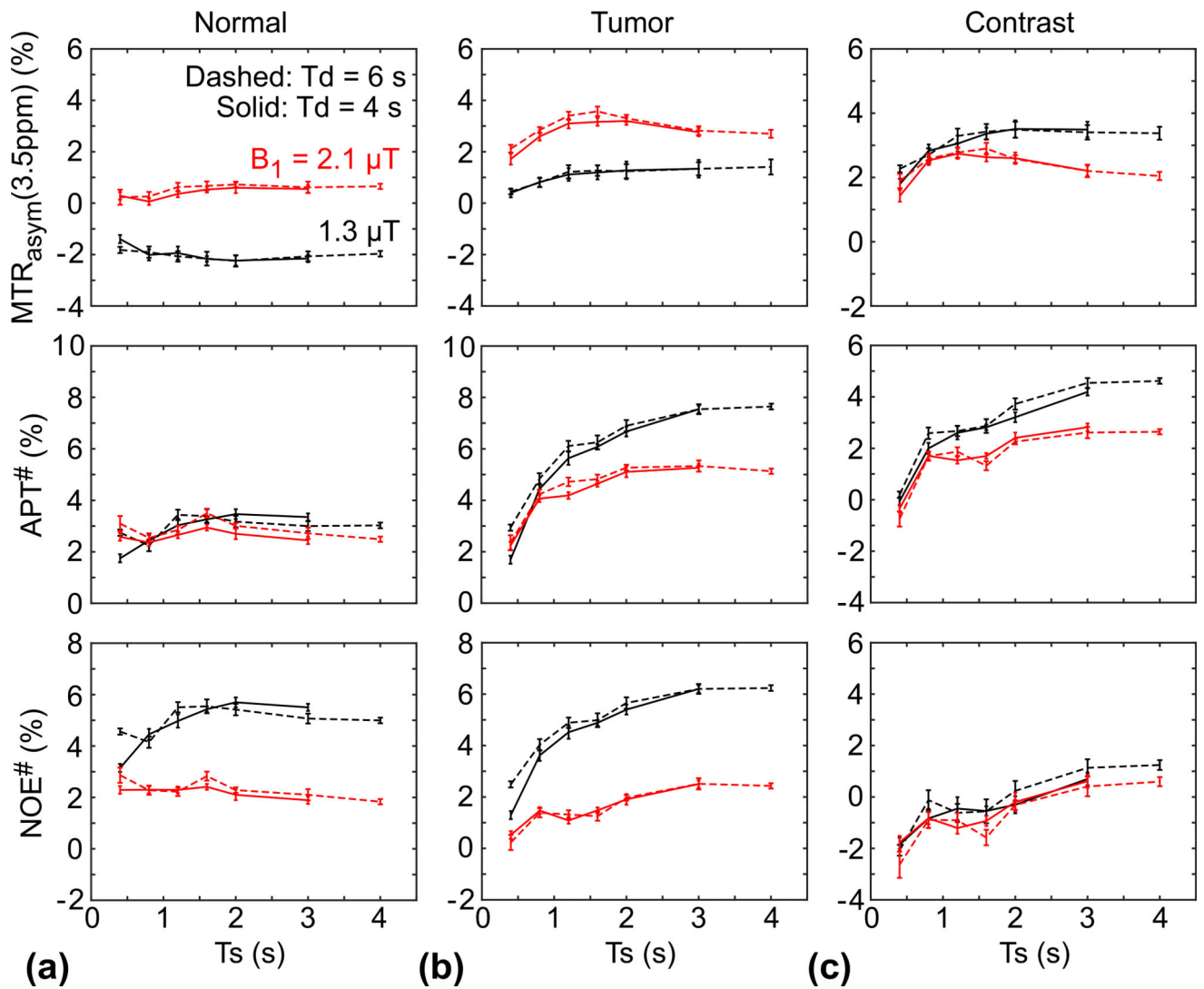
Figure 8.
Average MTR$_{asym}$(3.5ppm), APT$^{\#}$, and NOE$^{\#}$ signals of the normal (a) and tumor (b) tissues, and corresponding image contrasts between tumor and normal tissues (c).
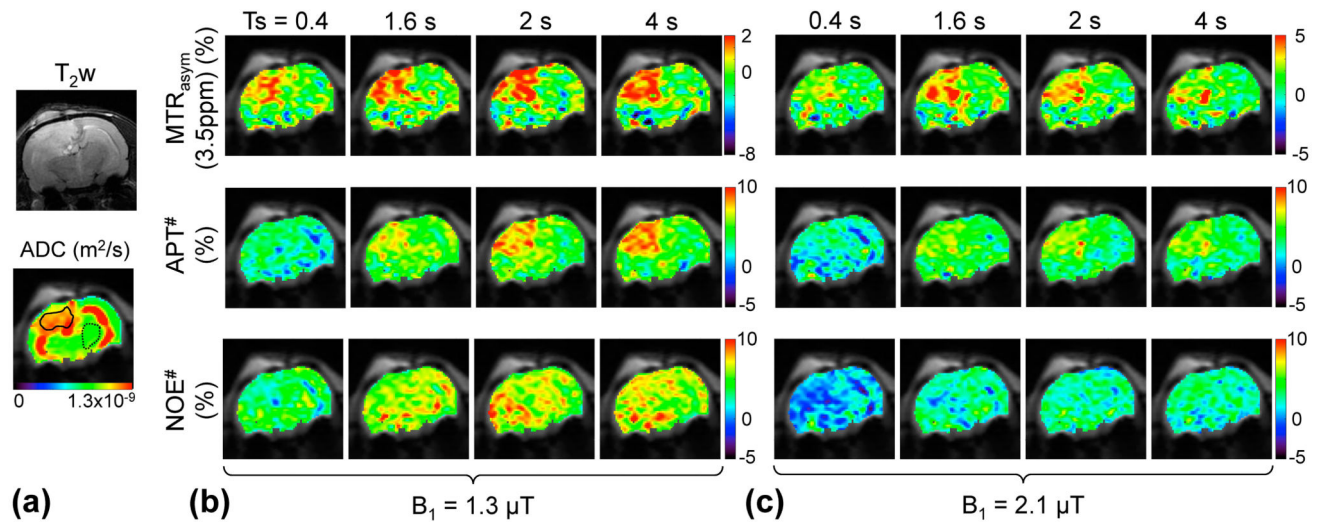
Figure 9.
T_2-weighted, ADC, MTR_{asym}(3.5ppm), $APT^{\#}$, and $NOE^{\#}$ maps with a relaxation delay of 6 s for a representative tumor-bearing rat.
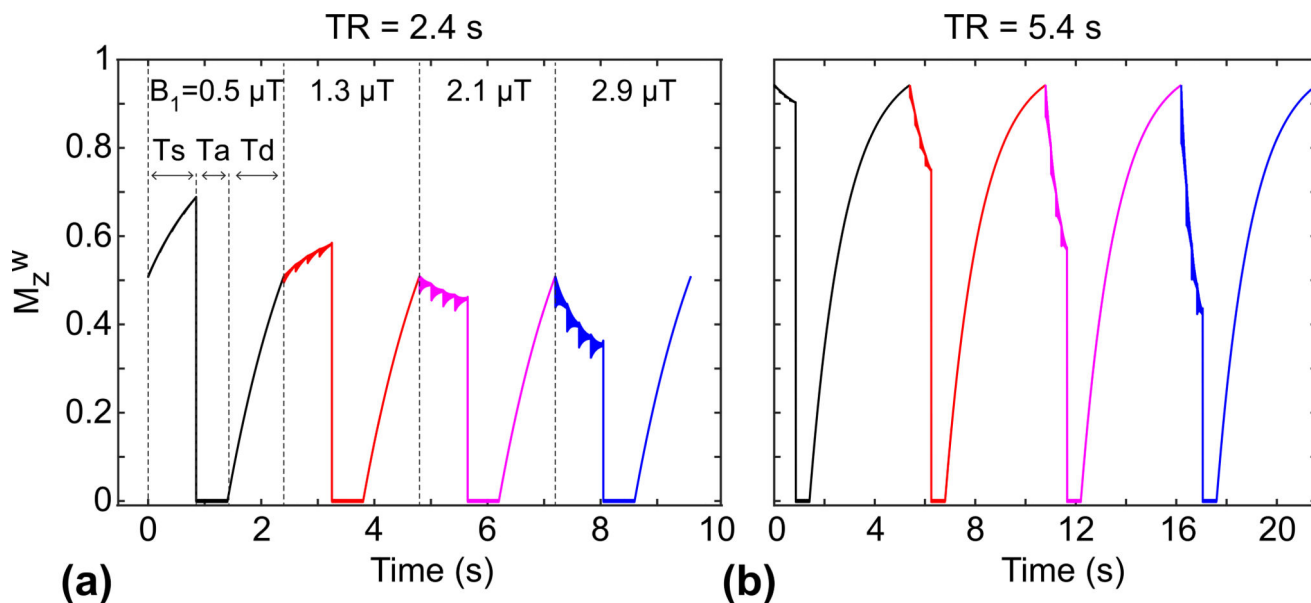
Figure 10.

The evolution of the longitudinal magnetization of the water (M_z^w) from a pulse-train TSE CEST sequence (after five dummy scans) under varied RF saturation powers, where B_1 = 0.5 (black), 1.3 (red), 2.1 (magenta), 2.9 μT (blue); Ts = 800 ms with a series of four block pulses (200 ms duration each), each followed by a crusher gradient (10 ms duration); TSE factor = 84; (a) TR = 2.4 s (Td = 1 s) and (b) TR = 4 s (Td = 4 s). Five-pool model parameters were used for the tumor case at 3 T.